NASA Technical Memorandum 4793

Wavelet Analyses of F/A-18 Aeroelastic and Aeroservoelastic Flight Test Data

Martin J. Brenner
Dryden Flight Research Center
Edwards, California

National Aeronautics and
Space Administration

Office of Management

Scientific and Technical
Information Program

1997

ABSTRACT

Time-frequency signal representations combined with subspace identification methods were used to analyze aeroelastic flight data from the F/A-18 Systems Research Aircraft (SRA) and aeroservoelastic data from the F/A-18 High Alpha Research Vehicle (HARV). The F/A-18 SRA data were produced from a wingtip excitation system that generated linear frequency chirps and logarithmic sweeps. HARV data were acquired from digital Schroeder-phased and sinc pulse excitation signals to actuator commands. Nondilated continuous Morlet wavelets implemented as a filter bank were chosen for the time-frequency analysis to eliminate phase distortion as it occurs with sliding window discrete Fourier transform techniques. Wavelet coefficients were filtered to reduce effects of noise and nonlinear distortions identically in all inputs and outputs. Cleaned reconstructed time domain signals were used to compute improved transfer functions. Time and frequency domain subspace identification methods were applied to enhanced reconstructed time domain data and improved transfer functions, respectively. Time domain subspace performed poorly, even with the enhanced data, compared with frequency domain techniques. A frequency domain subspace method is shown to produce better results with the data processed using the Morlet time-frequency technique.

NOMENCLATURE

a	wavelet scaling parameter
$[A,B,C,D]$	system state-space matrices
AOA	angle of attack
ASE	aeroservoelastic
CWT	continuous wavelet coefficient
da	finite interval of a
DFT	discrete Fourier transform
e	exponential function
f	center frequency of wavelet filter
$\mathscr{F}$	Fourier transform
FIR	finite impulse response
G	transfer function
h	wavelet basis function
H	Toeplitz matrix of Markov parameters
$H(\omega)$	Fourier transform of wavelet basis function
H_f	wavelet filter centered at f
HARV	High Alpha Research Vehicle
I	identify matrix
j	imaginary $\sqrt{-1}$
K	Kalman gain matrix
M	number of frequency data
MIMO	multi-input–multi-output
n	number of system states
N	number of time data
OBES	on-board excitation system
p	number system outputs

$[P,Q,S]$	matrices
SISO	single-input–single-output
SRA	Systems Research Aircraft
t	time
T	total time of wavelet analysis data
u	system input vector
U	block Hankel input matrix
V	block Hankel noise matrix
x	system state vector
X	state matrix
$x(t)$	analysis data in time domain
$X(\omega)$	analysis data in frequency domain
y	system output vector
Y	block Hankel output matrix
z	discrete frequency
Γ	extended observability matrix
τ	wavelet time shift parameter
ω	radian frequency

Superscripts

a	antisymmetric
s	symmetric

Subscripts

i,k	integer indices
o	noise subspace
s	signal subspace

Symbols

$\perp$	orthogonal complement
$\dagger$	pseudoinverse
$\hat{}$	estimate
$\overline{U}$	omission of first rows of matrix U
$\underline{U}$	omission of last rows of matrix U

INTRODUCTION

Envelope expansion of new or modified aircraft often necessitates structural stability testing to verify safety margins and to prevent catastrophic flutter. Inflight testing allows determination of aeroelastic or aeroservoelastic effects as a function of flight parameters. Flight data are acquired so stability estimation and system identification can be compared with analytic predictions. Any anomalies are regarded with care to guarantee maximum flight

safety. Because atmospheric turbulence is generally insufficient to determine modal characteristics, excitation systems are often essential to resolve stability trends from noisy measurements.

Flight flutter data processing attempts to analyze data characteristics in terms of timing, shape, amplitude, frequency, and duration of events in the data. These analyses have traditionally been addressed using classical Fourier techniques. However, Fourier methods are suspect due to the inherently transient nature of inflight aeroelastic dynamics. The infinite and at least locally-periodic waveform assumptions in Fourier analysis cannot adequately describe the intermittency, modulation (amplitude, phase, or frequency), nonperiodicity, non-stationariness, time-variance, or nonlinearity in the data.

This paper describes a novel filtering procedure which removes distortions from aeroelastic or aeroservoelastic (ASE) flight data. The filtering procedure builds upon and adapts the methods of wavelet transform analysis to the particular test data generated from structural excitation systems.

Wavelets are versatile harmonic analysis tools which combine time and frequency representations into localized waveforms. Given a segment of experimental data, the wavelet transform convolves a selected series of local waveforms with the data to identify correlated features, or patterns, in the signal. The resulting set of wavelet coefficients can be interpreted as multidimensional correlation coefficients. Features of shape, size, and location are naturally characterized by these waveforms and related coefficients.

The salient features of the original signal may be reconstructed by exploiting the redundancy of the wavelets in the continuous wavelet transform. Time-frequency components can be removed from these data by masking off the unwanted components (setting the corresponding wavelet coefficients to zero). This method is used to filter unwanted distortions and extract desired features from the input (excitation) and output (structural response) data. This *feature extraction* method offers advantages to traditional band-pass filtering or thresholding techniques in that it removes unwanted features while leaving desirable components intact.

By removing aspects of system inputs and outputs which are detrimental to linear identification methods, improvement of system identification is realized. Subspace identification methods have recently shown promise as being efficient, generally applicable, and robust. Experience with these methods will be discussed and comparisons made between transfer functions estimated with and without *feature processing*.

AIRCRAFT DESCRIPTIONS AND TEST PROCEDURES

Descriptions of the F/A-18 SRA and HARV follow. Flight flutter testing using a wingtip excitation system on the SRA is described in detail. High angle-of-attack aeroservoelastic research with the HARV is described using commands generated from the control system.

Systems Research Aircraft

The F/A-18 Systems Research Aircraft (SRA) is being flight tested at NASA Dryden Flight Research Center, Edwards, California, for primarily flight systems experiments. These tests include optical sensing, new actuation concepts, smart structures, and advanced airdata and flight control systems. A major left wing structural modification was done, however, on the SRA to allow testing of several hydraulic and electromechanical advanced aileron actuator concepts. Because the test actuators may be larger than the standard one, a fitting called a hinge-half (supporting the aileron hinge, the actuator, and a fairing) had to be replaced by larger and heavier items. Approximately 35 lb were added to the wing.

These SRA data were derived from flight flutter testing using a wingtip aerodynamic structural excitation system[1] at subsonic, transonic, and supersonic flight conditions.[2] Inputs were linear sinusoidal frequency sweeps, or

chirps, and logarithmic sweeps of the excitation system. Each wingtip exciter had a small fixed aerodynamic vane forward of a rotating slotted hollow cylinder (fig. 1). When the cylinder rotated, the aerodynamic pressure distribution on the vane generated a force. This force changed at twice the cylinder rotation frequency. The rotation direction of the cylinder could generate two force levels, low-force levels (at 25 percent open) or high-force levels (at 75 percent open). Exciters could be placed in various locations. Three possibilities were mid-wingtip, forward wingtip at the wingtip leading edge, or aft wingtip near the wingtip trailing edge (as pictured in figure 1).

Table 1 summarizes the matrix of test points for the SRA. Wingtip exciters were mounted on the SRA wingtip launcher rails in forward and aft positions, independently. They were operated in both low- and high-force modes for 15-, 30-, or 60-second forward and reverse frequency sweeps. A total of 260 test points were flown with exciters in one or more of the optional configurations at specified flight conditions. Linear and logarithmic sinusoidal sweeps of the exciter up to 40 Hz were used to excite the primary modes of interest in the 5 to 30 Hz range (table 2). Some sweeps were actually multiples of two or four shorter duration sweeps with no interrupt such as double (sweep up, then down) and quadruple (up-down-up-down) sweeps. Generally sweeps were performed for symmetric and antisymmetric excitation in each configuration.

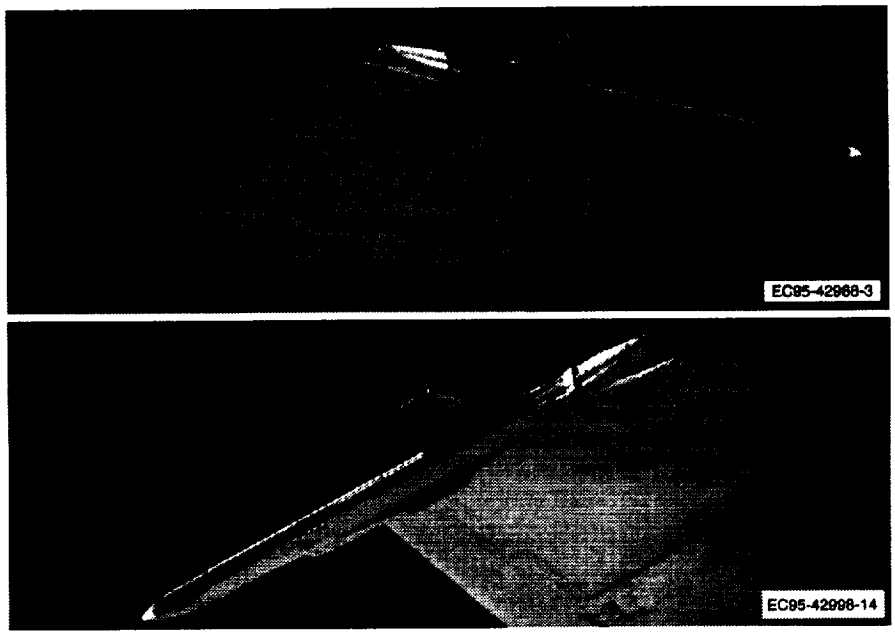

Figure 1. Wingtip exciter on F/A-18 SRA.

Table 1. SRA aeroelastic flight test matrix.

Mach number	0.54, 0.65, 0.70, 0.80, 0.85, 0.90, 0.95, 1.05, 1.2, 1.4, 1.6
Altitude, ft	10k, 30k, and 40k
Exciter position	Both forward, both aft, and left-aft/right-forward
Force	Low and high
Sweep	Linear and logarithmic
Duration, sec	15, 30, and 60
Range, Hz	3–12, 25–35, 3–35, 35–3, and 3–40
Multiple	Single, double, and quadruple contiguous sweeps per maneuver

Table 2. F/A-18 SRA with wingtip exciter: Calculated elastic modal frequencies.

Symmetric Mode	Hz	Antisymmetric Mode	Hz
Wing first bending	5.59	Fuselage first bending	8.15
Fuselage first bending	9.30	Wing first bending	8.84
Stabilizer first bending	13.21	Stabilizer first bending	12.88
Wing first torsion	13.98	Wing first torsion	14.85
Fin first bending	16.83	Fin first bending	15.61
Wing second bending	16.95	Wing second bending	16.79
Wing outboard torsion	17.22	Fuselage second bending	18.62
Fuselage second bending	19.81	Trailing-edge flap rotation	23.47
Trailing-edge flap rotation	23.70	Fuselage torsion	24.19
Stabilizer fore and aft	28.31	Launcher rail lateral	24.35
Wing second torsion	29.88	Stabilizer fore and aft	28.58
Aileron rotation	33.44	Wing second torsion	29.93
Aileron torsion	38.60	Aft fuselage torsion	37.80
Stab second bending, wing third bending	43.17	Wing pitch	39.18

High Alpha Research Vehicle (HARV)

Another F/A-18 aircraft (fig. 2) was modified at the NASA Dryden Flight Research Center to perform flight research at high angle of attack (AOA) using thrust vectoring and incorporating control law concepts for agility and performance enhancement, as well as providing data for correlation with computational fluid dynamics solutions. This vehicle is referred to as the High Alpha Research Vehicle (HARV)[3] throughout this report. As opposed to the SRA, the HARV was structurally very different from a standard F/A-18 aircraft, as can be seen by comparing the HARV modal data in table 3 with the SRA data in table 2.

Structural modifications included addition of Inconel® vanes in each engine exhaust for thrust vectoring. Corresponding ballast was added in the forward fuselage to maintain the center-of-gravity location. A research flight control system was incorporated for feedback control of aerodynamic surfaces and the vanes. An inertial navigation system was installed for AOA and angle of sideslip rate feedbacks, wingtip AOA vanes, and pressure probes (for airdata research purposes). Additional instrumentation was added for loads, vane temperatures, and structural dynamics.[4]

An important element of the HARV flight system was the onboard excitation system (OBES). This system was implemented to add programmed digital signals to the control system actuator commands for structural excitation. Inputs from 5 to 25 Hz were added to the stabilator, aileron, rudder, and pitch- and yaw-vectored thrust commands. Data were generated with OBES commands at 5° to 70° AOA[4] at 1 *g*. Accelerometers were located in the aircraft nose, vertical and horizontal tails, and wingtips.

®Inconel is a registered trademark of Huntington Alloy Products Div., International Nickel Co., Huntington, West Virginia.

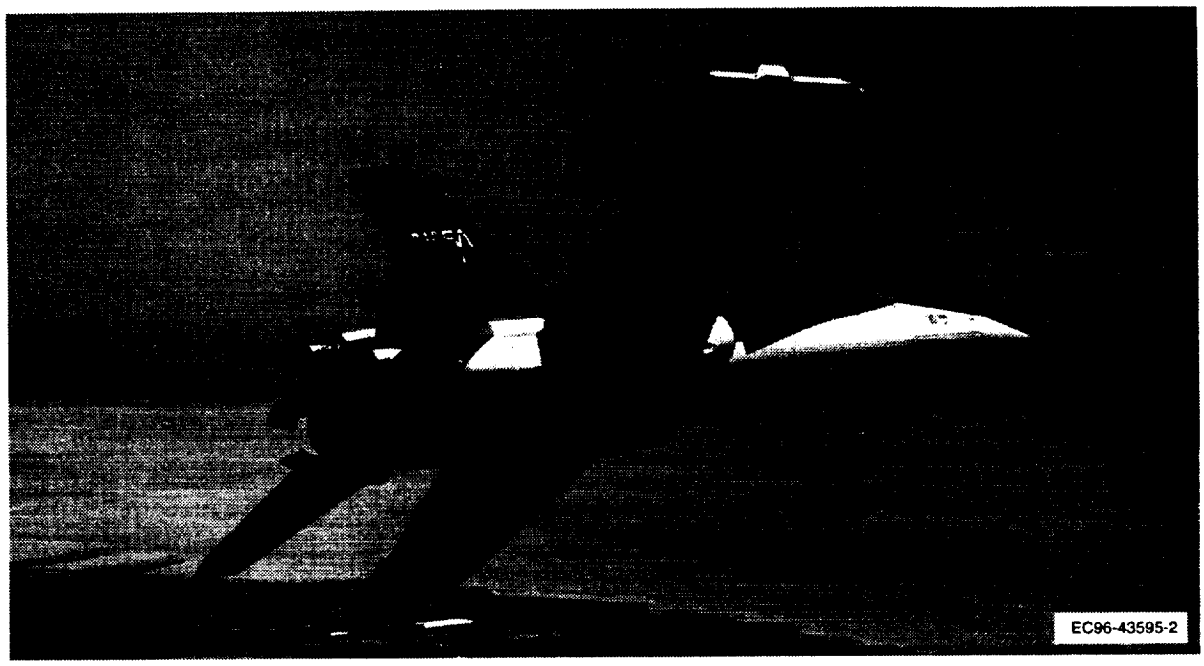

Figure 2. F/A-18 HARV.

Table 3. F/A-18 HARV calculated elastic modal frequencies.

Symmetric Mode	Hz	Antisymmetric Mode	Hz
Wing first bending	5.79	Fuselage first bending	7.13
Fuselage first bending	7.71	Wing first bending	8.75
Wing first torsion	11.68	Wing first torsion	12.03
Stabilizer first bending	13.73	Stabilizer first bending	13.63
Wing fore-aft	18.53	Wing fore-aft	15.18
Fin first bending	15.92	Fin first bending	15.71
Wing second bending	17.55	Fuselage first torsion	19.13
Fuselage second bending	15.87	Fuselage second bending	21.42
Exhaust vane rotation	22.10	Exhaust vane rotation	22.10
Inboard flap rotation	23.60	Inboard flap rotation	23.18
Wing outboard torsion	27.50	Fore-fuselage torsion	24.17

HARV data were generated from digital sinc $\left(\frac{\sin x}{x}\right)$ pulses and Schroeder-phased[5,6] inputs into control surface commands at generally high AOA. Sinc pulses and Schroeder-phased signals have a theoretically flat frequency response across a defined frequency band and are optimal for structural excitation because all modes are excited equally. Furthermore, Schroeder-phased signals have a minimal peak crest factor (difference between upper and lower bound of the power spectrum) amongst all signals with the same total power and are therefore preferred.

Schroeder-phased signals are multifrequency signals composed of a large number of harmonics equally spaced in frequency. Each harmonic is specified by a phase shift so that when they are summed the waveform has a low peak factor and fits a given power spectrum. It is represented by

$$x(t) = A\sum_{k}\cos\left(\omega t + \frac{\pi k^2}{N}\right) \tag{1}$$

where N is the number of data, and A is a specified amplitude to acquire maximum power under the saturation limits.

TIME-FREQUENCY ANALYSIS METHOD

This section illustrates the limitations of the Fourier transform as a tool for analysis of transient or short time period phenomena. The wavelet transform is offered as an alternative analysis tool, and the Morlet wavelet is selected as the wavelet basis function. Criteria for selecting the frequency width of the transform are discussed. Finally, a method for reconstructing the desirable features of the original signal from the wavelet coefficients and Morlet wavelet basis function is offered.

Wavelet Transform

Analysis of the frequency content of a signal using the Fourier transform results in a spectral representation that is a function of frequency. This transform is not localized in time. For a time-varying signal $x(t)$, however, a transform of the form

$$T(x(t)) = X(t, \omega) \tag{2}$$

is required to locate instantaneous frequencies. Such a transform is limited in resolution by the Heisenberg uncertainty principle

$$\Delta\omega \cdot \Delta t \geq 2 \tag{3}$$

Resolution problems resulting from the uncertainty principle can be minimized by extending the idea of the Fourier transform to a new time-frequency decomposition called the *wavelet decomposition*.[7] This decomposition performs an orthonormal projection of the signal onto a set of basis functions that are adapted to the required frequency resolution. The Continuous Wavelet Transform (*CWT*) is defined as

$$CWT(\tau, a) = \frac{1}{\sqrt{a}}\int_{-\infty}^{\infty} x(t)h^*\left(\frac{t-\tau}{a}\right)dt \tag{4}$$

where $h_{a,\tau}(t) = h\left(\frac{t-\tau}{a}\right)$ is the wavelet basis function, τ is the local time, and a is a scale or dilation parameter set to match the level of resolution desired. Wavelet transforms can be looked upon as the filtering of a signal through a bank of filters $h_{a,\tau}(t)$. These filters are band-pass with identical shape but with varying frequency width da centered around the frequencies of interest. Note that the $h_{a,\tau}(t)$ are not orthogonal because they are redundant (defined for continuous a and τ). With the *CWT* the time resolution is arbitrarily good at high frequencies, and the frequency resolution becomes arbitrarily good at low frequencies (within the limits of the uncertainty principle) because da/a is constant. Time-frequency analyses attempt to minimize the effects of these resolution problems by using *a priori* knowledge of the signal properties or adapting the resolution to the signal.[8,9]

Selection of Wavelet Basis

Aeroelastic and aeroservoelastic excitation data are essentially short-time sinusoidal, so the selection of a wavelet basis function should encompass this characteristic. Therefore, the Morlet wavelet[10]

$$h(t) = \frac{1}{\sqrt{2\pi}} e^{-\frac{t^2}{2}} e^{-i\omega t} \tag{5}$$

was chosen as the basis function because of its clear interpretation in the frequency domain (Gaussian window) and time domain (locally periodic waveform) for the analysis of vibration data. Figures 3(a) and 3(b) show real and imaginary components of the Morlet wavelet. Figure 3(c) shows a Fourier representation of the real part.

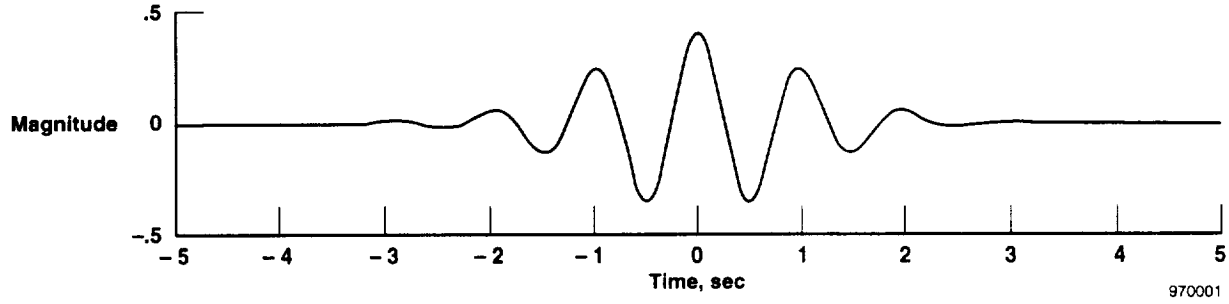

(a) Real part (top).

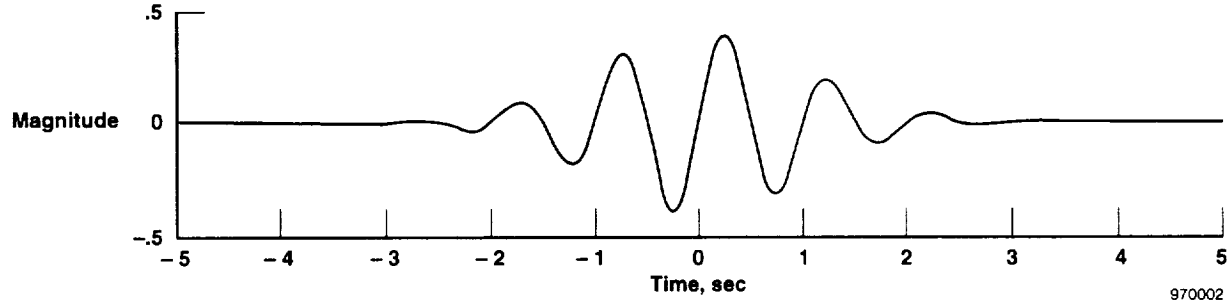

(b) Imaginary part (middle).

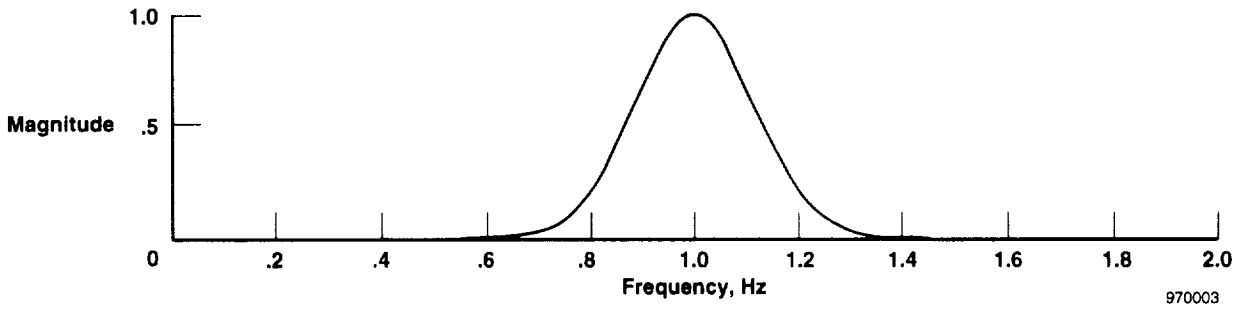

(c) Fourier transform of real part (bottom).

Figure 3. Morlet continuous wavelet transform.

For analysis of the SRA data composed of linear frequency sweeps where the rate of change is constant over the whole time interval, a constant resolution is required along the entire time-frequency domain. Hence, the chosen time-frequency transform uses nondilated (a = constant) Morlet wavelets as functions onto which the data are projected. For a selected frequency and frequency resolution, the wavelet transform convolves the corresponding Morlet filter with the signal to produce the wavelet coefficients.

Resolution Criteria

A tradeoff between time and frequency resolution is used to select the appropriate frequency resolution of the filter. In the case of the sweeps considered here, the frequency varies from ω_1 to ω_2 in T seconds. Assuming a desired resolution of $\Delta\omega$ in frequency, the time resolution Δt is actually given by the time localization of this frequency by

$$\Delta t = \frac{T}{\omega_2 - \omega_1}\Delta\omega \tag{6}$$

From the Heisenberg uncertainty principle (eq. (3)), we have

$$\Delta\omega^2 = 2\,\frac{\omega_2 - \omega_1}{T} \quad \text{and} \quad \Delta t^2 = 2\,\frac{T}{\omega_2 - \omega_1} \tag{7}$$

For a typical linear sweep from 0 to 30 Hz in 30 sec, these relations give $\Delta t = \sqrt{2}$ sec, and $\Delta\omega = \sqrt{2}$ Hz. These values will be used to determine the frequency width of the Morlet filters.

Time-Frequency Filtering and Signal Reconstruction

In the frequency domain, the wavelet coefficient corresponding to a Morlet filter with center frequency f is

$$CWT(\omega, f) = \mathcal{F}(CWT(t, f)) = X(\omega) \cdot H_f(\omega) \tag{8}$$

where the Fourier transform of the Morlet wavelet is

$$H_f(\omega) \equiv H(\omega, f) \tag{9}$$

The complex Morlet basis function from equation (5) presents problems because it should have no group delay (real Fourier representation) and no phase distortion. For example, when reconstructing the original time domain signal from a bank of complex Morlet filters, phase distortion results. Therefore, only the real part of the Morlet wavelet is used to ensure that the transform $H_f(\omega)$ is real, and signal reconstruction is in-phase with the original signal. The Fourier transform of the real part

$$H_f(\omega) = e^{-(\omega - f)^2} - e^{-\omega^2 - f^2} \tag{10}$$

is shown in figure 3(c). Convolution and inverse Fourier transform operations produce the desired time-frequency coefficients

$$CWT(t, f) = \mathcal{F}^{-1}(X(\omega) \cdot H_f(\omega)) \tag{11}$$

where $X(\omega)$ and $H_f(\omega)$ are the Fourier transforms of signal and Morlet wavelet, respectively. This real Morlet filter bank provides a finite impulse response (FIR) linear phase filter for each center frequency f and maintains phase consistency between the original signal and some type of reconstruction.

Assuming that n wavelet basis functions are to be used to perform the signal reconstruction, equation (8) is used to construct the FIR filter bank. For a given frequency ω_0, the wavelet coefficients are related to the original signal spectrum by

$$\begin{bmatrix} CWT(\omega_0, f_1) \\ \vdots \\ CWT(\omega_0, f_n) \end{bmatrix} = X(\omega_0) \begin{bmatrix} H_{f_1}(\omega_0) \\ \vdots \\ H_{f_n}(\omega_0) \end{bmatrix} \tag{12}$$

This equation is solved for $X(\omega_0)$ using the pseudoinverse at every frequency ω_0

$$\hat{X}(\omega_0) = \begin{bmatrix} CWT(\omega_0, f_1) \\ \vdots \\ CWT(\omega_0, f_n) \end{bmatrix} \begin{bmatrix} H_{f_1}(\omega_0) \\ \vdots \\ H_{f_n}(\omega_0) \end{bmatrix}^{\dagger} \tag{13}$$

and is inverse transformed to get the time domain reconstruction $\hat{x}(t)$.

This procedure will be used subsequently to filter unwanted distortions and extract desired features from the input excitation and output structural response data from the SRA and HARV aircraft. These feature-filtered data will then be used to compute cleaned signals for transfer functions and subspace identification algorithms. Figure 4 shows an outline of the entire procedure.

SIGNAL PROCESSING IN THE TIME-FREQUENCY DOMAIN

Transfer functions are routinely used in aeroelastic and aeroservoelastic analyses to acquire state-space representations of the system modal dynamics and to predict flutter boundaries with damping trends or other advanced techniques.[11,12] Traditional Fourier transform methods often disguise important features in the data from

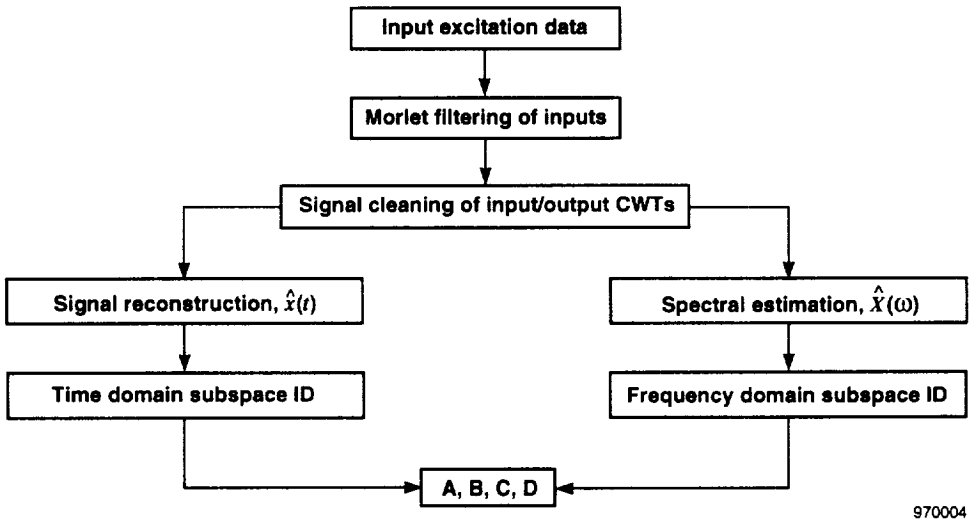

Figure 4. Time-frequency Morlet feature-filtered system identification (ID) procedure.

averaging and windowing. To circumvent these problems, a recipe using the wavelet-based feature extraction filter is employed to estimate cleaner transfer functions based on time-frequency localization. Figure 4 shows a schematic of the entire procedure.

- Feature filter by masking the dominant harmonic band in the inputs and performing the same procedure to the outputs. The resulting input–output pairs are from a strictly linear system.
- Localize the relevant frequency content by filtering each input–output signal with a bank of narrow band-pass FIR filters centered around each ω_i.
- Localize the relevant time information by windowing each band-pass-filtered signal around the time point where a filtered input has maximum amplitude. The relevant information at frequency ω_i is assumed to be localized in time. Energy outside the chosen time window at identical frequencies is considered as noise.
- Apply equation (13) for every windowed input–output pair at each ω_0.
- Reconstruct time signals $\hat{x}(t)$ for time domain identification or derive transfer functions using the spectral input–output pairs of $\hat{X}(\omega)$.

Figure 5 shows an example of what the Morlet filter can do beyond standard Fourier techniques. The top four plots are derived from standard Fourier techniques, from one exciter (left) to accelerometer output and other exciter (right) to the same output. The bottom four plots are the corresponding Morlet feature-filtered results. Improvement is obvious with the Morlet-processed data in identifying modal peaks from the noise and establishing well-defined phase response.

A comparison is made between the Morlet wavelet filter and signal analysis with a discrete Fourier transform (DFT) using a sliding window in figure 6. The signal is a linear sweep measured from the SRA exciter vane as the aeroelastic system input. The sliding DFT is computed for the same frequency resolution as the Morlet filter bank. A Hanning window is applied, and its real part is plotted as a function of time. The result is a discrete short-time Fourier transform. A magnitude and time-frequency representation of the sliding DFT is commonly referred to as a spectrogram. As shown, the results seem comparable, but the sliding DFT suffers from increased smearing in the resolution of the harmonics (lower left corner) and at the end of the sweep. It is well known that the inverse sliding transform suffers from loss of resolution, or "time smearing,"[13] and is also computationally inefficient. Furthermore, the short-time Fourier transform suffers from fixed frequency resolution for all times; whereas, the wavelet filter bank approach allows adjustments in time and frequency resolution pertaining to the signal characteristics.

APPLICATION TO F/A-18 SRA AEROELASTIC DATA

A procedure for deriving transfer functions from the SRA wingtip excitation data is described. Time-frequency analyses are applied to this data for enhancing transfer functions and improving system identification methods such as subspace identification.

Transfer Function Derivation

Estimation of transfer functions from the SRA data was predominantly used to identify state-space matrices for prediction of flutter boundaries. Because the input was corrupted by exciter vane anomalies and inconsistencies, extracting information relevant to linear system identification and considering the rest as being detrimental to linear stability estimation was necessary. Therefore, assuming the system to be identified is linear, the extraneous energy at frequencies other than the excitation frequency is considered as corruptible unmodeled dynamics, noise, or both. Along the main harmonic of the input will also be noise (as with output), but the signal-to-noise ratio is assumed to be sufficiently high to mask the majority of the noise corruption.

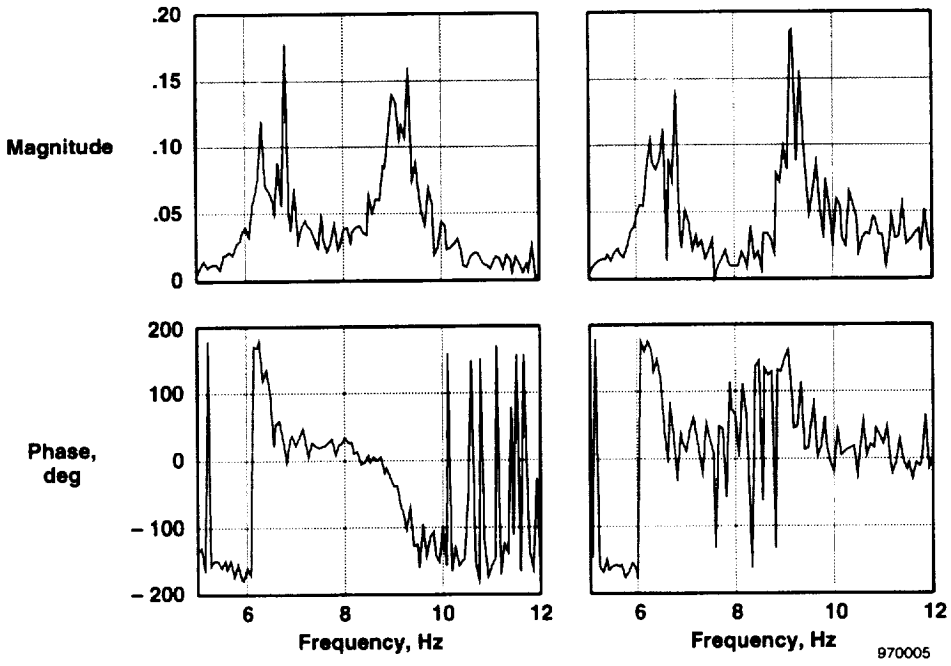

(a) Classical Fourier transfer functions.

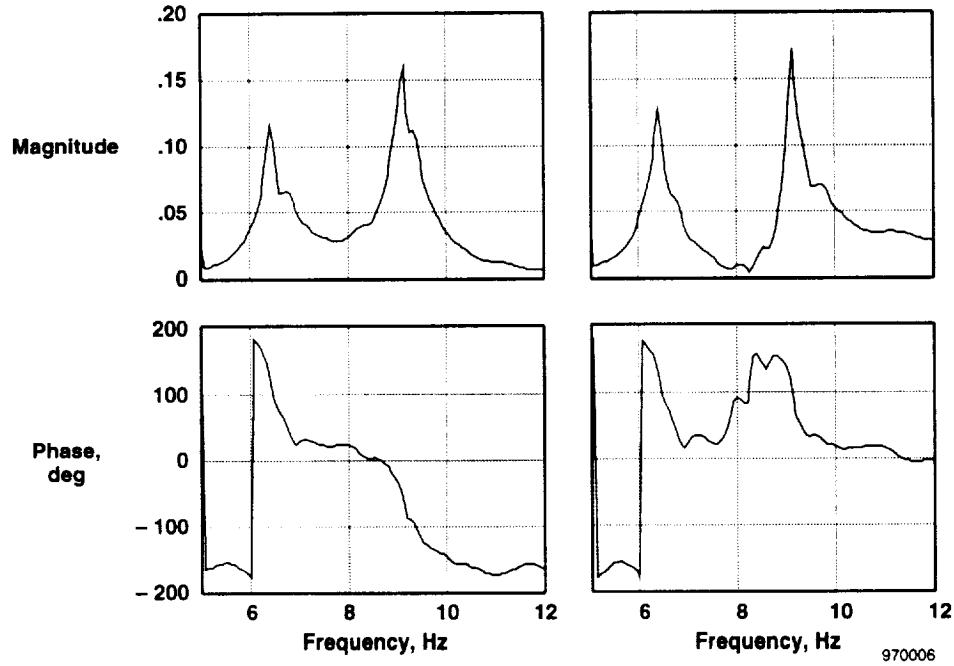

(b) Corresponding time-frequency generated transfer function.

Figure 5. Transfer functions computed with classical Fourier technique and time-frequency method. Left exciter input to accelerometer output (left column). Right exciter input to accelerometer output (right column).

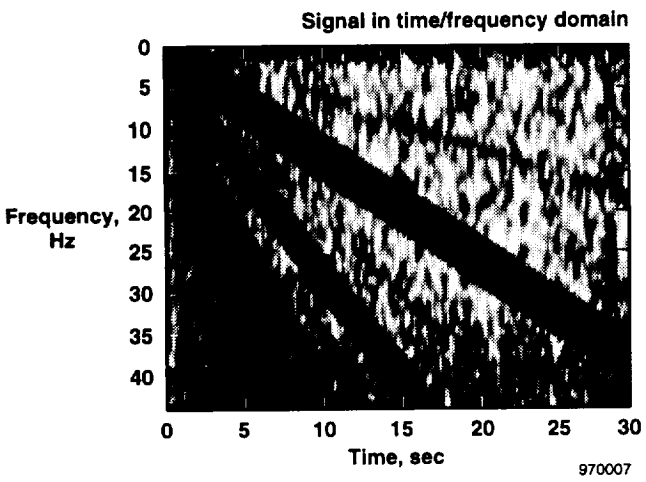

(a) Morlet continuous wavelet transform.

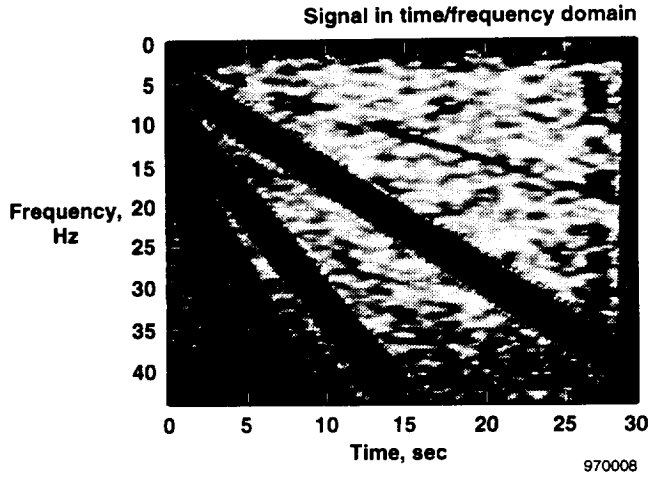

(b) Discrete short time Fourier transform (right)

Figure 6. Morlet continuous wavelet transform compared to the discrete short-time Fourier transform of SRA exciter data.

The procedure for SRA transfer function derivation from the symmetric and antisymmetric exciter inputs is as follows:

- Compute the Morlet-filtered *CWT* coefficients of the inputs $u_1(\omega_i)$ and $u_2(\omega_i)$ from each of the two exciter vanes (operating simultaneously for symmetric u^s and antisymmetric u^a sweeps) at each filtered center frequency ω_i.
- Compute $y(\omega_i)$ for each output y^s and y^a at each filtered center frequency ω_i.
- Estimate transfer functions $G_1(\omega_i)$ and $G_2(\omega_i)$ from each exciter vane input to the output:

$$\begin{bmatrix} y^s(\omega_i) \\ y^a(\omega_i) \end{bmatrix} = \begin{bmatrix} u_1{}^s(\omega_i) & u_2{}^s(\omega_i) \\ u_1{}^a(\omega_i) & u_2{}^a(\omega_i) \end{bmatrix} \begin{bmatrix} G_1(\omega_i) \\ G_2(\omega_i) \end{bmatrix} \tag{14}$$

- and for each ω_i

$$\begin{bmatrix} G_1(\omega_i) \\ G_2(\omega_i) \end{bmatrix} = \begin{bmatrix} u_1{}^s(\omega_i) & u_2{}^s(\omega_i) \\ u_1{}^a(\omega_i) & u_2{}^a(\omega_i) \end{bmatrix}^{-1} \begin{bmatrix} y^s(\omega_i) \\ y^a(\omega_i) \end{bmatrix} \tag{15}$$

Time-Frequency Analysis

A demonstration of applications using wavelet time-frequency maps, called *scalograms*, for data enhancement in system identification of SRA structural dynamics follows. In figure 7(a), a scalogram showing the original input signal of a linear frequency sweep from the exciter is displayed. A primary harmonic is clearly seen as well as other dynamics and noise. The main harmonic is the desired part of the signal because it tracks the programmed input to the exciter. The actual input to the exciter is much more complicated due to nonlinear aerodynamics and distributed loading across the exciter vane. By creating a mask around the main harmonic *CWT* of the input and applying it to the *CWT* of the output signal (accelerometer, fig. 8), the dynamic properties of the system can be identified. Figure 7(b) represents the masked input *CWT*.

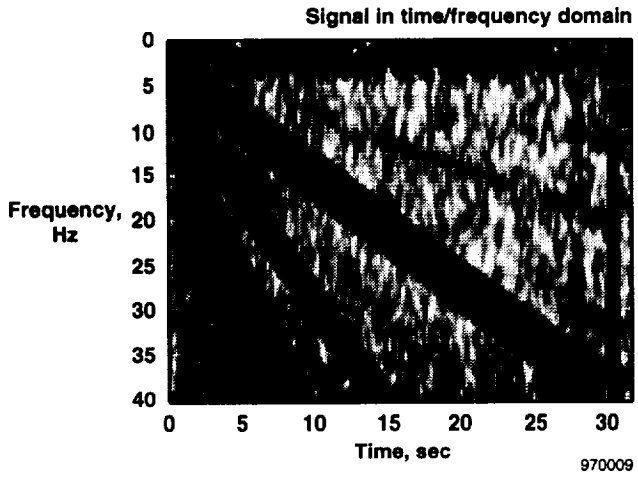

(a) Scalogram of original SRA exciter signal.

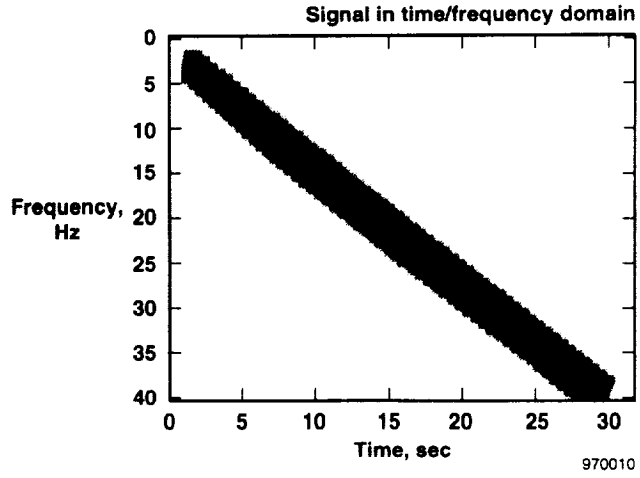

(b) Scalogram of cleaned SRA exciter signal by feature filtering the CWT.

Figure 7. Morlet scalograms of original input and cleaned input.

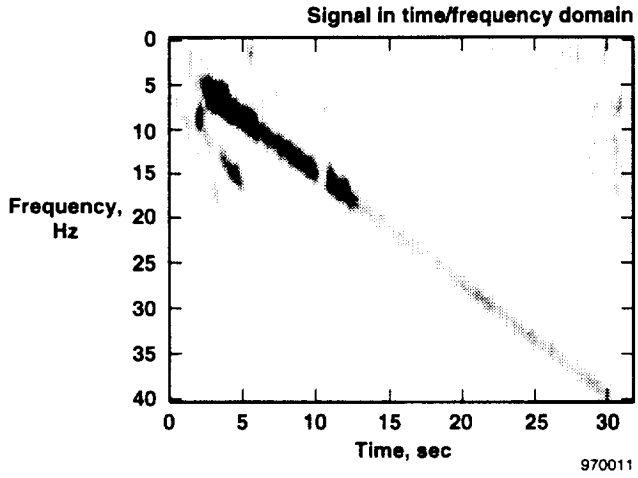

(a) Scalogram of original accelerometer response.

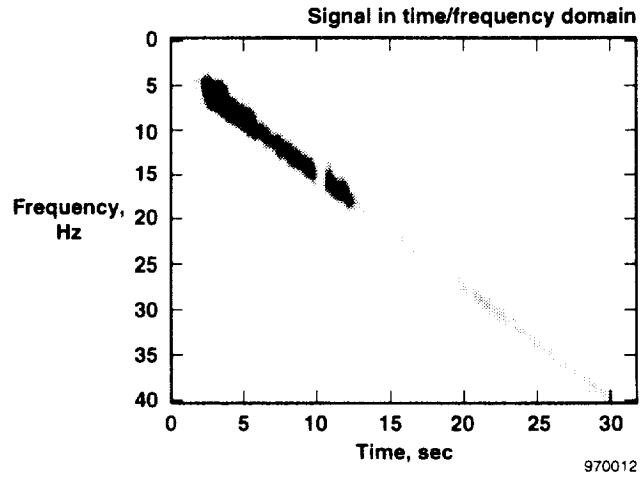

(b) Scalogram of cleaned accelerometer response.

Figure 8. Morlet scalograms of raw and cleaned accelerometer output.

Signal reconstruction uses the redundancy of the wavelets to estimate a time signal which the *CWT* best approximates. The real transform $H_f(\omega)$ assures an in-phase reconstruction compared with the original signal. Figure 9 shows the original (unprocessed) and reconstructed clean (processed) signals from figure 7. The same procedure is performed on left and right exciter inputs and an output accelerometer signal to generate transfer functions in figure 10. Note the extreme contrast between the original results (fig. 10(a)) and the cleaned (fig. 10(b)) transfer functions, especially in phase. These plots show the improved noise removal in the cleaned data for distinguishing modes below 20 Hz, and the potential for dramatic differences in phase between input and output responses upon cleaning. Estimation of a state-space system can then be performed using the enhanced data from the cleaned *CWT* and an algorithm, such as subspace identification.[14–17]

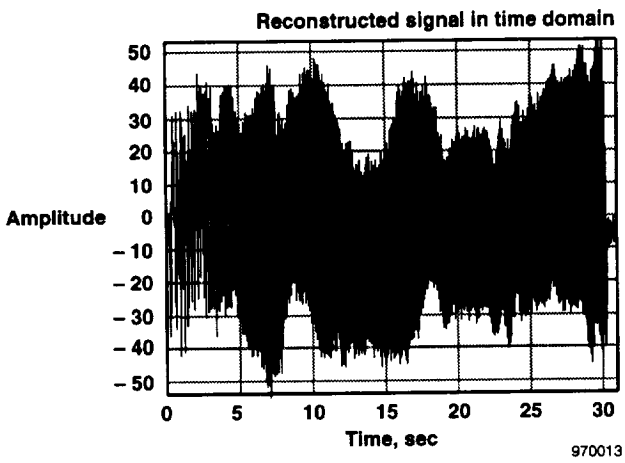

(a) Reconstructed signal of original accelerometer response.

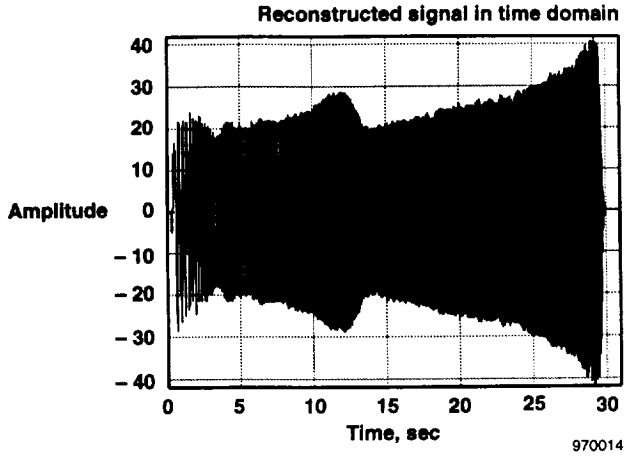

(b) Reconstructed signal of cleaned accelerometer response.

Figure 9. Original signal and cleaned signal reconstruction.

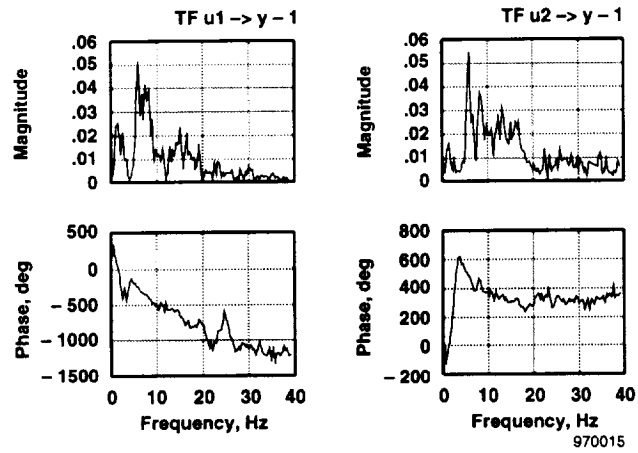

(a) Transfer functions using raw time-frequency data. Left exciter (left column) and right exciter (right column) to accelerometer output.

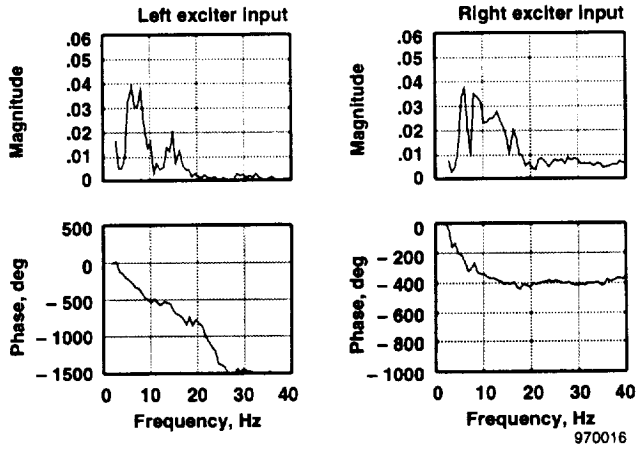

(b) Transfer functions using cleaned time-frequency data. Left exciter (left column) and right exciter (right column) to accelerometer output.

Figure 10. Transfer functions using raw and cleaned time-frequency data.

An example of filtering the undesirable features of complicated input–output signals using the time-frequency representation will be a double logarithmic sweep from the SRA excitation system. Figures 11 and 12 show planar and three–dimensional scalograms of the original and desired sweeps. Harmonics from the strain gauge input measurement can be readily detected in figures 11(a) and 12(a). The harmonics indicate nonlinear exciter vane response from the rotating slotted cylinders at the wingtips, which is deemed undesirable for subsequent linear state-space identification methods. Therefore, the input signal is modified by extracting the desired time-frequency map from the scalogram (figs. 11(b) and 12(b)) and reconstructing the time domain input signal.

As exemplified, general maps in the time-frequency plane can be effectively filtered. Also, such signals would be very difficult to threshold because the harmonic wavelet coefficients are of comparable amplitude. Hence, a method of automating this feature filtering process will generally not benefit from typical thresholding schemes.[18]

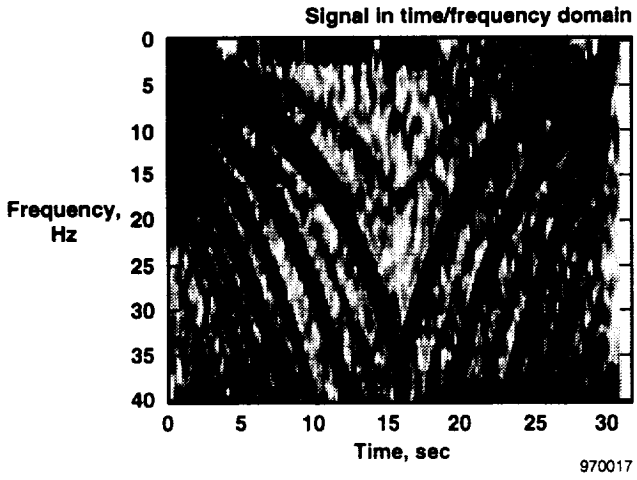

(a) Original input.

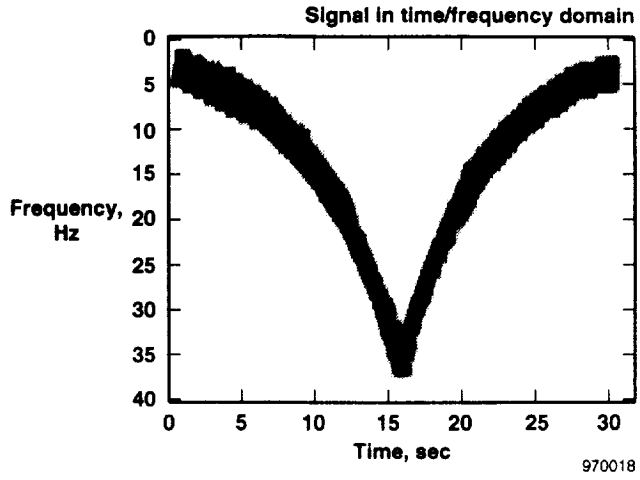

(b) Cleaned input.

Figure 11. Scalograms of original double-sweep logarithmic input and cleaned input.

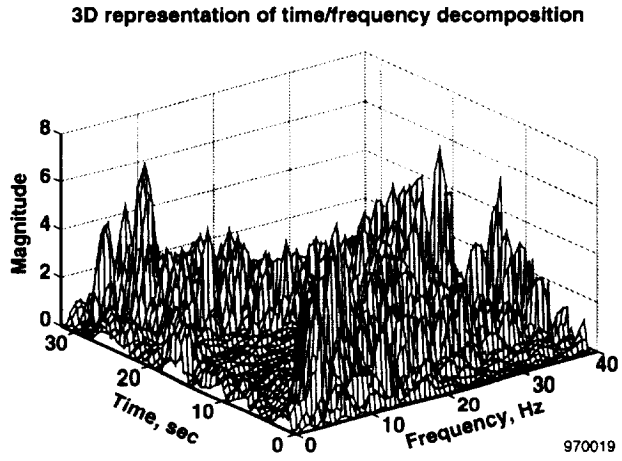

(a) Original input.

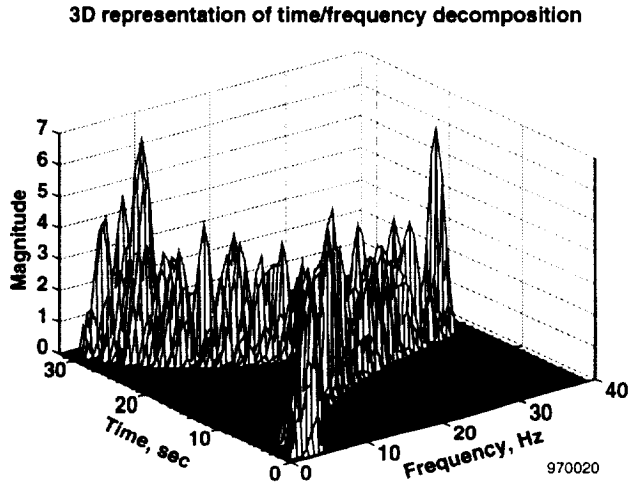

(b) Cleaned input.

Figure 12. Three-dimensional scalograms of original double-sweep logarithmic input and cleaned input.

Subspace System Identification

Estimated transfer functions with a classical Fourier method and the time-frequency localization approach are compared in figure 5. The cleaned transfer functions are clearly superior in illuminating the modal responses relative to the noise. This distinct difference between the two approaches would considerably influence a system identification procedure.

Example plots in figure 13 compare SRA transfer functions from a typical aeroelastic data set with transfer functions generated from the frequency domain algorithm[15] outlined in the appendix. Transfer functions are from exciter inputs to an accelerometer output and are derived from unprocessed and processed time-frequency data. Matches between unprocessed data and the subspace estimate are in figure 13(a), and figure 13(b) matches processed

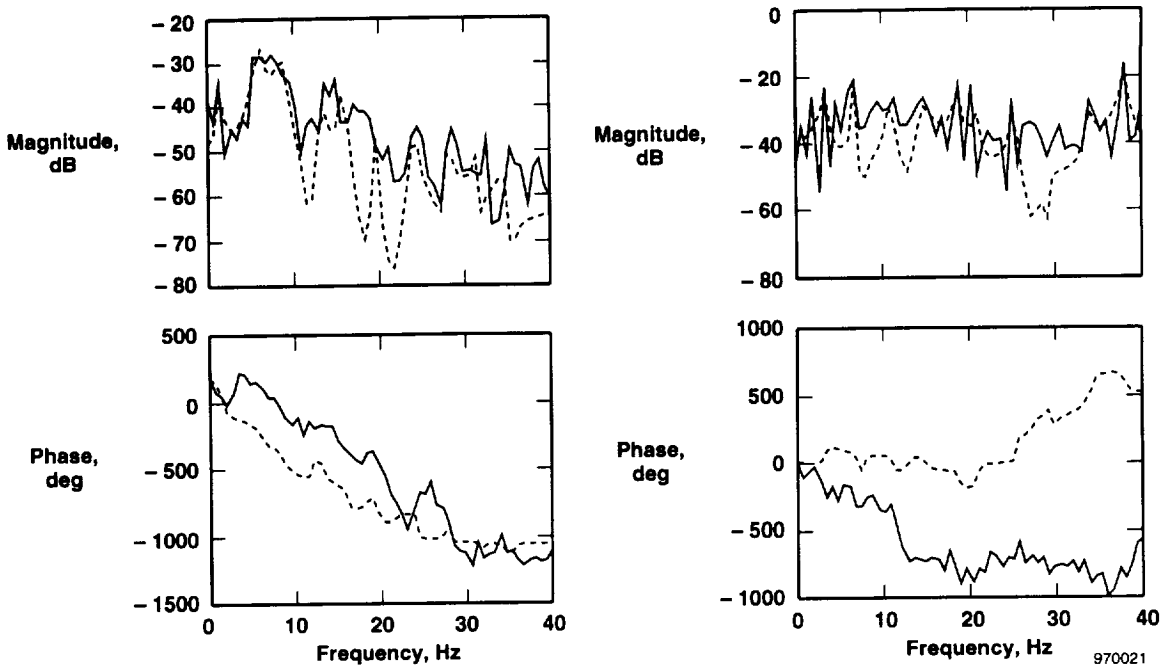

(a) Transfer functions derived from raw time-frequency data.

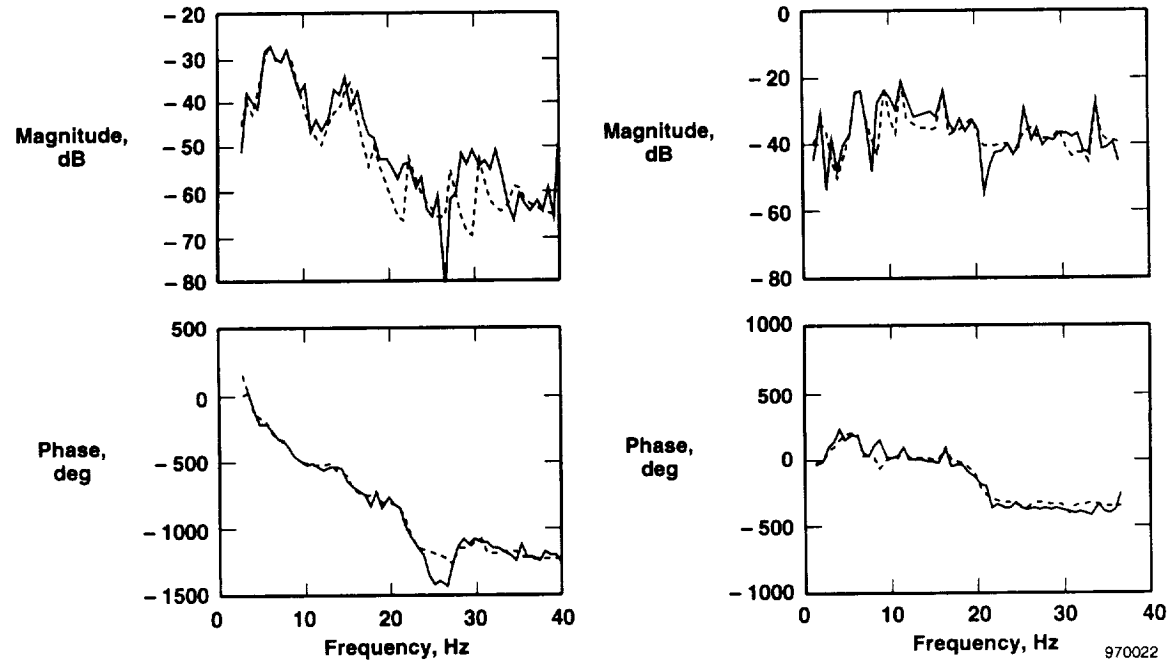

(b) Transfer functions derived from cleaned time-frequency data.

Figure 13. Discrete-time frequency domain subspace identification results. Solid lines are transfer functions from exciter input to accelerometer output computed with raw (a) and cleaned (b) time-frequency data. Dashed lines are transfer function estimates from a frequency domain subspace identification algorithm processing the solid line data.

data with subspace estimates. The solid line on these plots are transfer functions derived from the time-frequency procedure, and the dashed lines are subspace identification estimates. Agreement is consistently better between processed transfer functions and the identification, compared to the original transfer functions, thereby providing an increased degree of confidence in the system quadruple estimates when using the feature-filtered data.

APPLICATION TO F/A-18 HARV AEROSERVOELASTIC DATA

The excitation signals used for generating aeroservoelastic excitation data are described. Morlet decompositions of data from these maneuvers are used for analysis.

Excitation Mechanisms

Schroeder-phased harmonic signals were compared to sinc-pulses $\left(\frac{\sin x}{x}\right)$ because linear and logarithmic sweeps are deficient at low and high frequencies, respectively. OBES Schroeder-phased and sinc-pulsed signals were chosen to excite the HARV at the same range of flight conditions of 1 g, 5° to 70° AOA and 30,000 ft altitude. Analysis of the Schroeder-phased data compared to linear sweep and sinc-pulse data at the same conditions is reported in reference 19.

Figure 14 shows a Schroeder wave input to the aileron and the resulting aileron position and roll rate. Figure 15 shows a sinc-pulse input to the aileron with position and roll rate. These signals were input to the surfaces sequentially in the following order within 70 sec: symmetric stabilator, differential stabilator, ailerons, rudders, pitch thrust vector vanes, and yaw thrust vector vanes.

Decomposition of Schroeder-Phased Harmonic Data

Figure 16(a) shows an example Morlet scalogram of a 5 to 25 Hz Schroeder input into the pitch thrust-vectoring command at 10° AOA. The nature of the time-frequency response is the sum of two distinct sweeps, one sweeping the low frequencies followed by the high frequency sweep with little overlap. All frequencies from 5 to 25 Hz are being excited equally. The time-frequency-filtering procedure used to analyze the SRA data is applied in figure 16(b), and subsequent analysis applies accordingly. In contrast to the SRA data, the OBES inputs are relatively clean because they are generated digitally by the flight system. Figure 17 shows the corresponding transfer functions of structural response from the OBES inputs of pitch and yaw thrust vectoring. The procedure enhances the modes near 15 Hz and above relative to the other frequencies, which is justified from figure 18 where the output accelerometer response scalogram is plotted. The response is dominated by energy around 15 Hz and above relative to other frequencies, with little response below 15 Hz. Note the order of magnitude difference.

Decomposition of Sinc-Pulse Data

Figure 19 shows scalograms of sinc pulses. In contrast to the Schroeder-phased signal, sinc functions contain the majority of their energy in a small amount of time. It seems that processing of these data is unnecessary because nearly all the energy is concentrated in a well-defined area in the time-frequency plane localized in time. Figure 20 shows corresponding transfer functions of structural response from the OBES inputs of pitch and yaw thrust vectoring. Noise in the spectral response is drastically reduced in figure 20(b) compared to figure 20(a). In figure 20(a), some difficulty exists in discriminating modal response from spurious noise peaks; in figure 20(b), the modal response is more distinct. These transfer functions demonstrate that considerable improvement in data quality is achieved by time-frequency filtering. Time localization of the signal degrades the frequency response unless this property is exploited in the analysis. In figures 19(b) and 20(b), the time-localized energy is extracted from the input–output signals to define a much cleaner frequency response from which to perform system identification. Note the order of magnitude difference in gain between raw and cleaned magnitude responses. Also note that the responses for the same flight condition at 10° AOA and same input–output signals are very different between the two types of excitation, Schroeder-phased and sinc-pulsed, either unprocessed or processed.

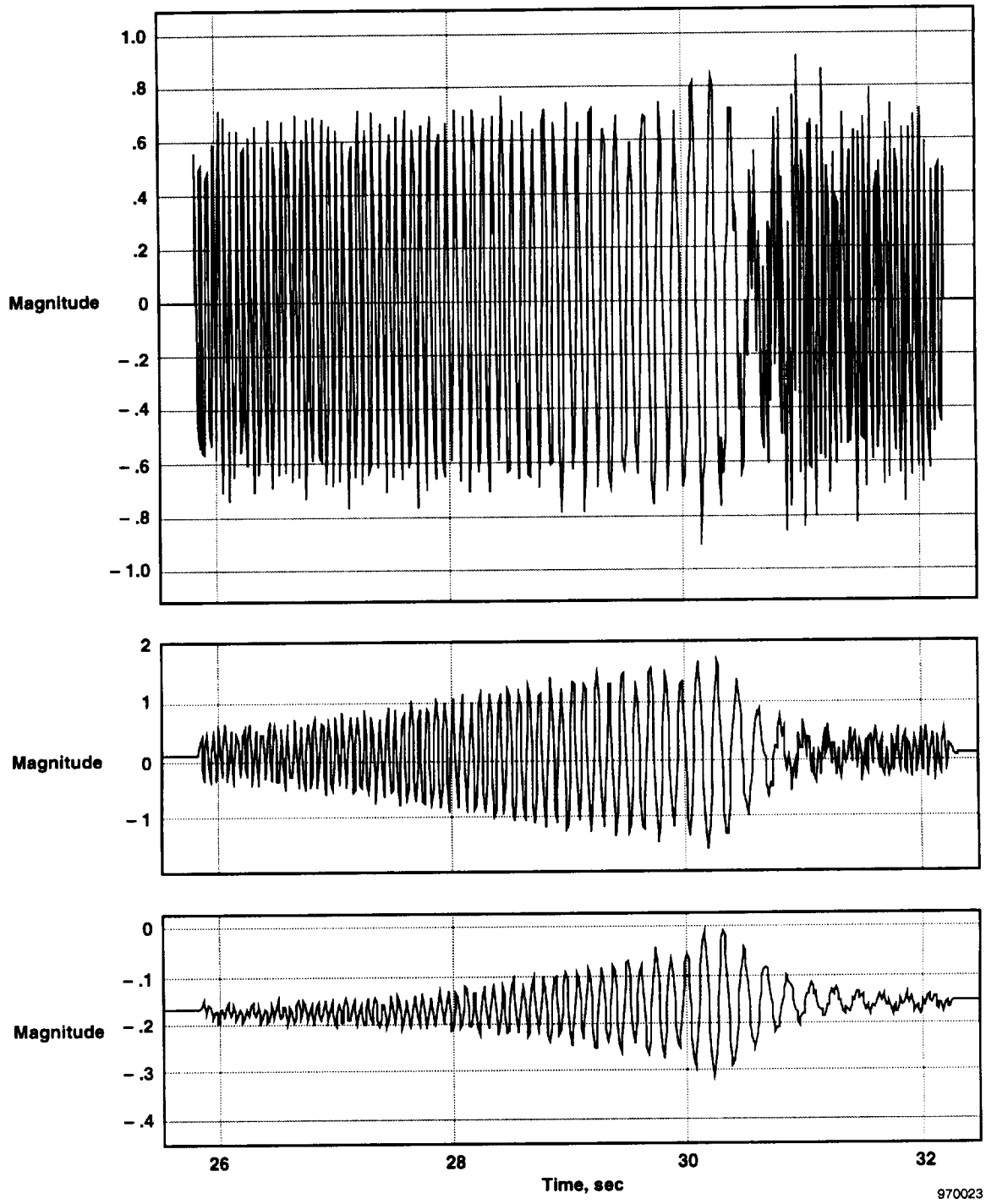

Figure 14. Example Schroeder-phased harmonic aileron command input (top), aileron position (middle), and roll rate (bottom).

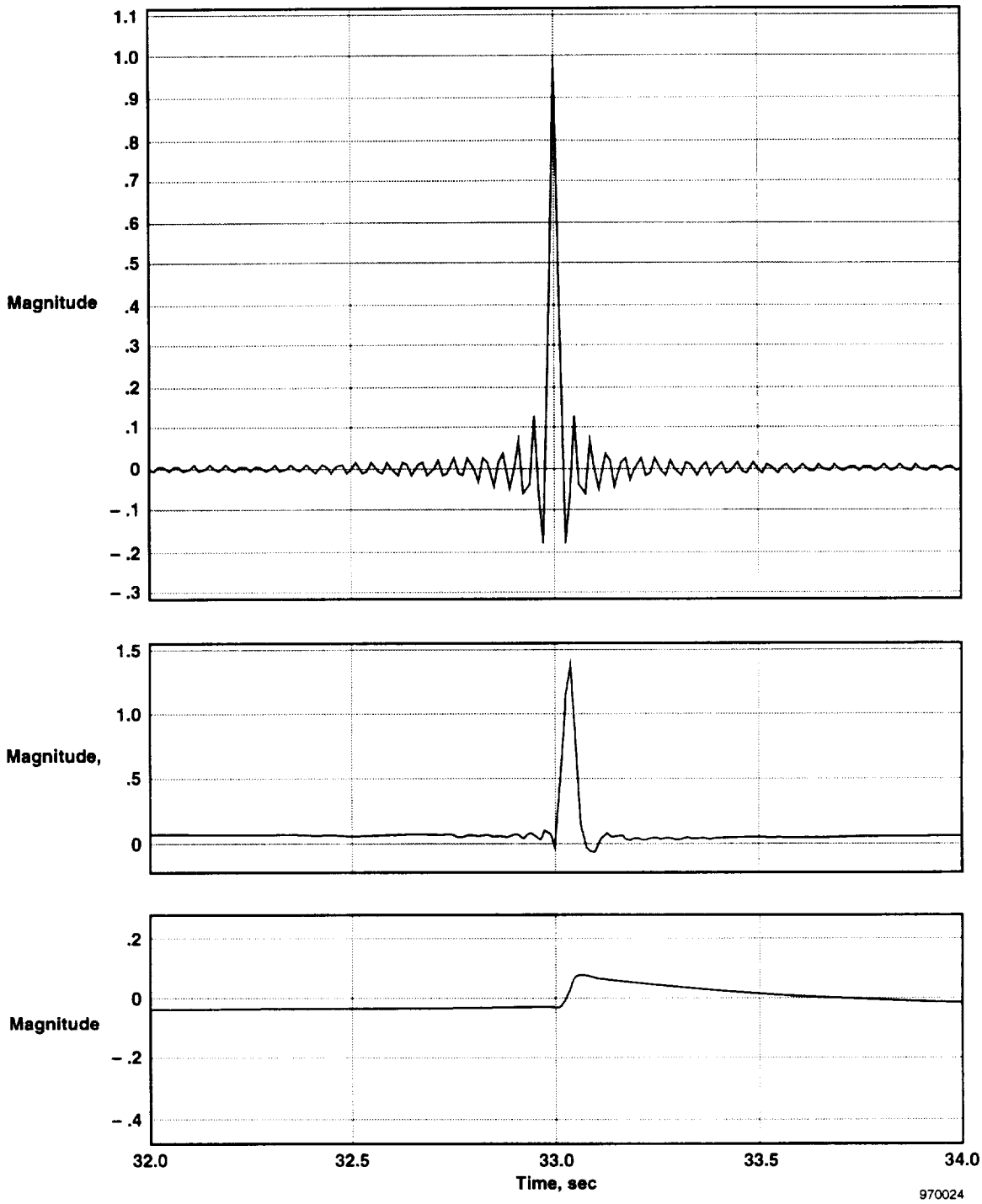

Figure 15. Example sinc-pulse aileron command input (top), aileron position (middle), and roll rate (bottom).

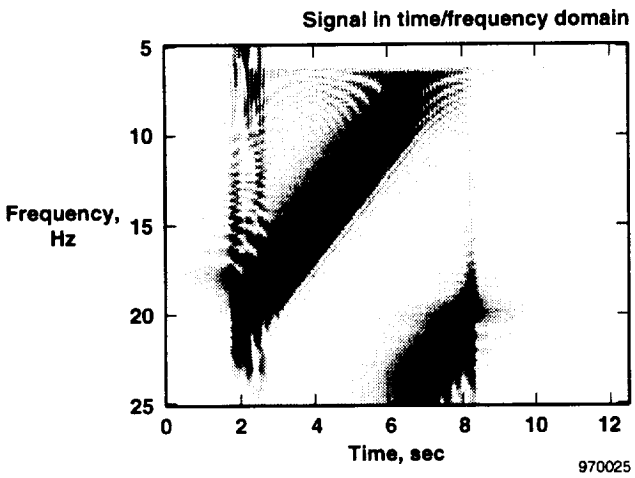

(a) Raw scalogram.

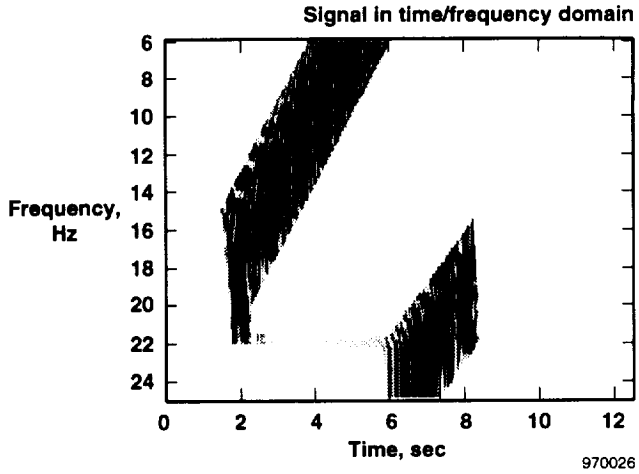

(b) Cleaned scalogram.

Figure 16. Morlet scalograms of Schroeder-phased harmonic input.

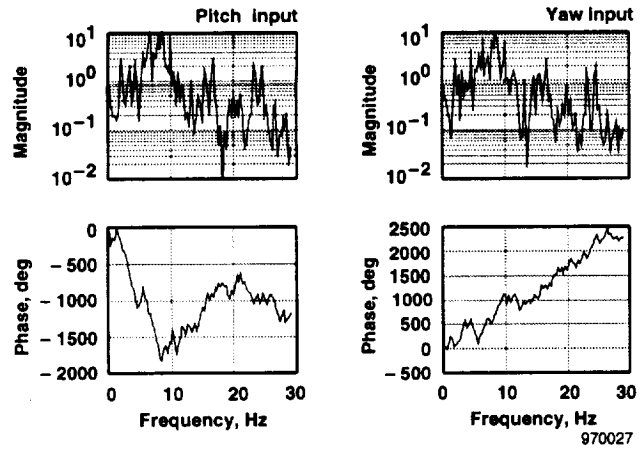

(a) Transfer functions derived from raw time-frequency data (left). Pitch thrust vector input (left column) and yaw thrust vector input (right column).

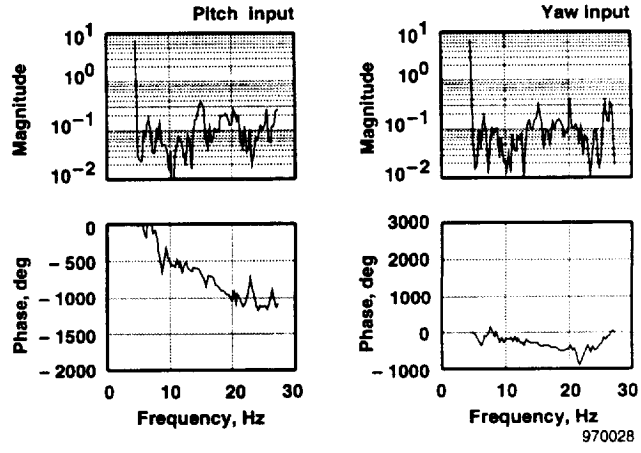

(b) Transfer functions derived from cleaned time-frequency data (right). Pitch thrust vector input (left column) and yaw thrust vector input (right column).

Figure 17. Transfer functions from raw and cleaned Schroeder-phased data.

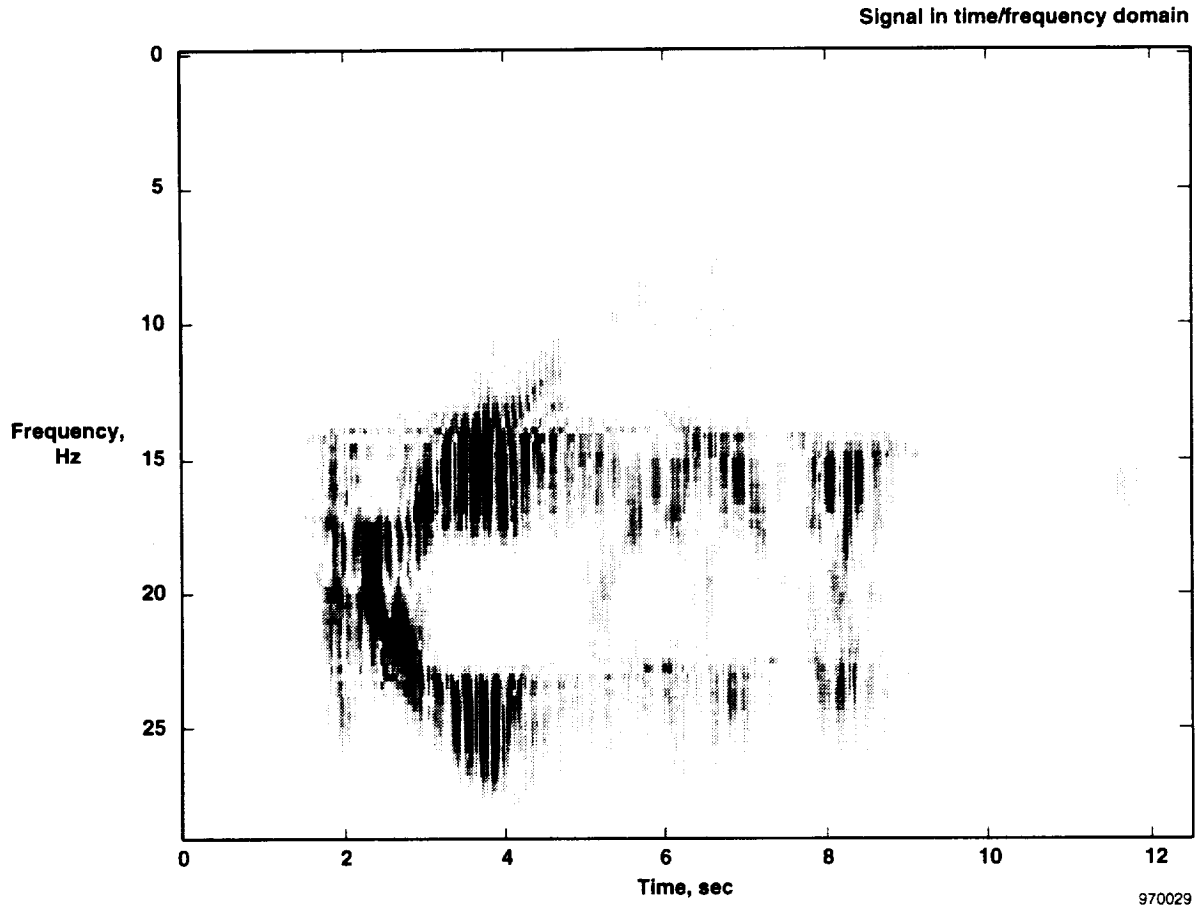

Figure 18. Accelerometer response scalogram from Schroeder-phased input.

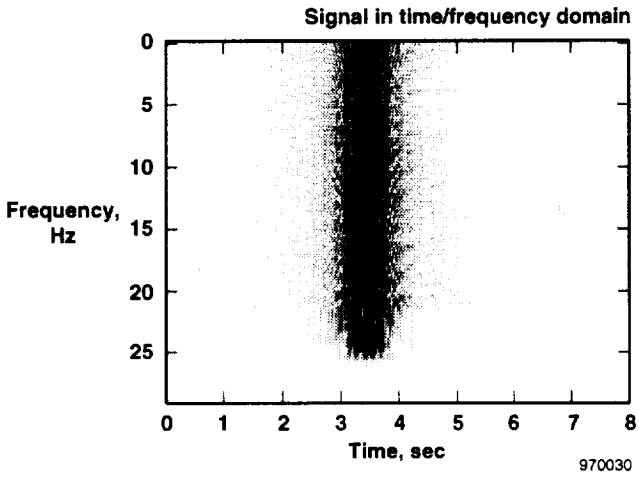

(a) Raw scalogram.

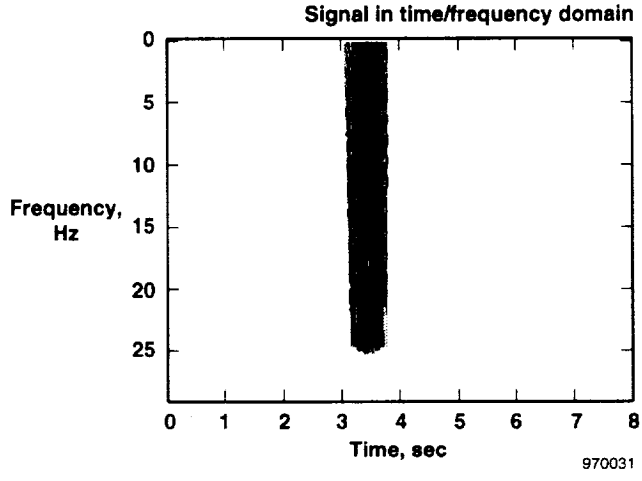

(b) Cleaned scalogram.

Figure 19. Morlet scalogram of sinc-pulsed input.

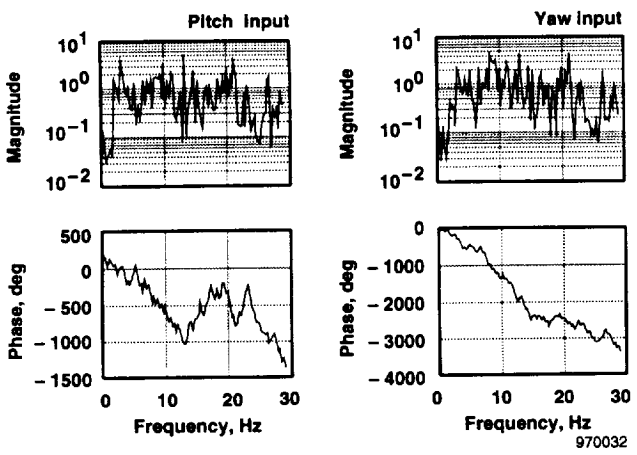

(a) Transfer functions derived from raw time-frequency data. Pitch thrust vector input (left column) and yaw thrust vector input (right column).

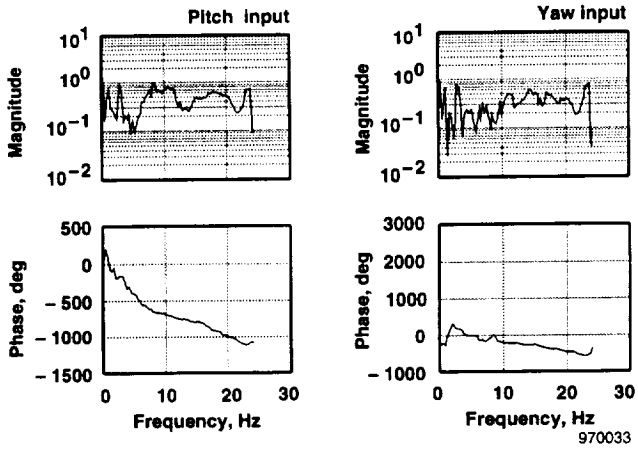

(b) Transfer functions derived from cleaned time-frequency data. Pitch thrust vector input (left column) and yaw thrust vector input (right column).

Figure 20. Transfer functions from raw and cleaned sinc-pulsed data.

CONCLUSIONS

Multiresolution analyses of flight vibration data on two F/A-18 aircraft were performed with nonorthogonal, nondilated Morlet wavelets. This procedure offered enhanced capabilities for time-frequency feature extraction and filtering and for subsequent system identification. Such a time-frequency approach allows improved visualization and understanding of the signal information content. Noise and other distortion dynamics can be identified, reduced, or eliminated. Automated thresholding would be difficult in the majority of situations when distortion dynamics are significant relative to the signal content. This proposed approach succeeds when standard threshold techniques are inappropriate. Identification schemes used to extract modal data, state-space representations, or stability boundaries demonstrate improved performance with these procedures.

APPENDIX

An outline of system identification is presented in time and frequency domains. Proposed advantages and experiences with algorithms using structural excitation data is described.

Subspace Identification of System Quadruple

Subspace identification methods attempt to find a linear, time-invariant, state-space realization

$$x_{k+1} = Ax_k + Bu_k + \omega_k \tag{16}$$

$$y_k = Cx_k + Du_k + v_k \tag{17}$$

based on the input vector sequence u_k and output sequence y_k. The state vector x_k is not directly observed, so it is only identifiable to within a similarity transformation. White noise vectors ω_k and v_k are zero-mean process and measurement noise, respectively. The state-space model identification problem is then as follows:

> Given N input–output samples $\{u_k, y_k\}$ of the unknown system, find a consistent estimate of the state-space quadruple $[A,B,C,D]$ up to a similarity transformation T. Determine the Kalman gain K such that the output of the estimated system
>
> $$x_{k+1} = Ax_k + Bu_k + K(y_k - Cx_k) \tag{18}$$
>
> $$y_k = Cx_k + Du_k \tag{19}$$
>
> is the minimum variance one-step ahead prediction of the recorded output.

Subspace algorithms are regarded as powerful modern techniques for linear system identification because of numerous advantages. For example,

- They are noniterative, nonparametric, and linear.
- They are numerically robust algorithms.
- They produce nonparametric state-space models.
- Their MIMO and SISO algorithms are identical.
- They have both time and frequency domain versions.
- They have model insensitivity to matrix perturbations.
- There is good performance for identification of high-order (structural) systems.

For these reasons, the following algorithms are outlined with emphasis on experiences in performance, using data processed with Morlet wavelet filtering.

Block Hankel matrices that play an important role in subspace methods are

$$U = \left[\frac{U_p}{U_f}\right] \begin{bmatrix} u_1 & u_2 & \cdots & u_{N-2k+1} \\ u_2 & u_3 & \cdots & u_{N-2k+2} \\ \vdots & & \ddots & \vdots \\ u_k & u_{k+1} & \cdots & u_{N-k} \\ u_{k+1} & u_{k+2} & \cdots & u_{N-k+1} \\ \vdots & & \ddots & \vdots \\ u_{2k} & u_{2k+1} & \cdots & u_N \end{bmatrix} \tag{20}$$

where U_p and U_f designate past and future samples. A similar construction is made for the output matrix Y. The extended observability matrix is defined as

$$\Gamma = \begin{bmatrix} C \\ CA \\ \vdots \\ CA^{s-1} \end{bmatrix} \tag{21}$$

Fundamental to subspace algorithms is the following matrix equation

$$Y = \Gamma X + HU + V \tag{22}$$

where Y, U, and V are Hankel matrices formed with the output samples, input samples, and noise, and H is the Toeplitz matrix of Markov parameters

$$H = \begin{bmatrix} D & 0 & 0 & \dots & 0 \\ CB & D & 0 & \dots & 0 \\ CAB & CB & D & \dots & 0 \\ \dots & \dots & \dots & \ddots & \dots \\ CA^{s-2}B & CA^{s-3}B & CA^{s-4}B & \dots & D \end{bmatrix} \tag{23}$$

The following types of subspace identification methods were compared for this study: strictly time domain,[16] combined time and frequency domain,[11] and frequency domain.[14,15,20] Time domain algorithms had the worst performance, especially in extracting B and D matrices, so a different approach was proposed. The A and C matrices were derived from the time domain data, then the B and D matrices were computed from matching the state-space model with estimated transfer functions. This approach gave better results than using a strictly time domain version in getting the B and D matrices, especially when using the filtered transfer functions from the Morlet time-frequency method.[11] Finally, two algorithms using frequency domain data were tried to take advantage of the improved transfer functions. All algorithms will be outlined here for completeness.

Time Domain Algorithm

Because the transfer function estimates are based on at least two distinct data sequences from the SRA data (symmetric and antisymmetric), a method was used to determine system A and C matrices from multiple data sets.[21] Briefly, A and C are derived from the following technique (C is p by n).

- Find P such that $P = \Gamma Q$ and rank(P) = rank(Γ). In the noise-free case ($V = 0$), $P = YU^{\perp}$ because $HUU^{\perp} = 0$ in equation (22) ($\perp$ denotes an orthogonal complement). For two data sets, $P = [P_1\ P_2] = \Gamma[Q_1\ Q_2]$. The following steps remain the same.
- Decompose $P = USV$, where $S = \begin{pmatrix} S_1 & 0 \\ 0 & 0 \end{pmatrix}$, and $U = \begin{pmatrix} U_1 \\ U_2 \end{pmatrix}$ are rank(P).
- Evaluate: $A = \overline{U}_1^{\dagger}\underline{U}_1$ where $\overline{U}_1(\underline{U}_1)$ respectively omit the first (last) p rows of U_1, and $\dagger$ denotes pseudoinverse. C is the first block of U_1.
- Premultiply (2) by $\Gamma^{\perp}$, so $\Gamma^{\perp}\Gamma = 0$ and post-multiply by $U^{\dagger}$ leading to a least squares solution of $\begin{bmatrix} B \\ D \end{bmatrix}$.

Combined Time and Frequency Domain Algorithm

In the combined time-frequency domain algorithm, the B and D matrices are found from discrete transfer function $G(z_k)$, where $z_k = e^{j\omega_k}$ and $\omega_k = \frac{\pi k}{M}$ for M data, $k = 0, \ldots, M$

$$G(z_k) = \left[C(z_k I - A)^{-1} I\right]\begin{bmatrix} B \\ D \end{bmatrix} \tag{24}$$

for all frequencies ω_k, the least squares solution separating real and imaginary is

$$\begin{bmatrix} B \\ D \end{bmatrix} = \begin{bmatrix} C(z_1 I - A)^{-1} & I \\ C(z_2 I - A)^{-1} & I \\ \vdots & \vdots \\ C(z_M I - A)^{-1} & I \end{bmatrix}^{\dagger} \begin{bmatrix} G(z_1) \\ G(z_2) \\ \vdots \\ G(z_M) \end{bmatrix} \tag{25}$$

Frequency Domain Algorithm

Frequency domain algorithms[14,15,20] are similar in context. In particular, one method[15] starts with the premise that the transfer function G of the system has a real-valued impulse response. As a result, data on $[0,\pi]$ can be extended to $[\pi,2\pi]$ by taking the complex conjugate and continuing as follows.

- Extend transfer function samples to the full unit circle: $G_{M+k} := G^{*}_{M-k}, k-1, \ldots, M-1$.
- Define the real block Hankel matrix: $2M$-point inverse DFT $\hat{h}_i = \frac{1}{2M}\sum_{k=0}^{2M-1} G_k e^{\frac{j2\pi ik}{2M}}$.

  $\hat{H} := \begin{bmatrix} \hat{h}_1 & \cdots & \hat{h}_r \\ \vdots & \ddots & \vdots \\ \hat{h}_q & \cdots & \hat{h}_{q+r-1} \end{bmatrix}$ where $(q,r) > n$ and $q + r \le 2M$.
- Compute the SVD: $\hat{H} = \hat{U}\hat{\Sigma}\hat{V}^T$.
- Determine system order n by inspecting singular values and partitioning: $\hat{H} = [\hat{U}_s \hat{U}_o]\begin{bmatrix} \hat{\Sigma}_s & 0 \\ 0 & \hat{\Sigma}_o \end{bmatrix}\begin{bmatrix} \hat{V}_s^T \\ \hat{V}_o^T \end{bmatrix}$.
- Determine system matrices $\hat{A}$ and $\hat{C}$ as $\hat{A} = (\underline{\hat{U}}_s)^{\dagger}\bar{\hat{U}}_s$ and C is the first p-block of $\hat{U}_s$.
- Solve least squares, as above, for B and D.

Other algorithms use auto- and cross-spectral data in the same framework[14] or identify a Laplace domain $[A,B,C,D]$ from discrete transfer function data ω_k using numerically well-conditioned Forsythe polynomials.[20] These frequency domain algorithms perform well for high-order structural systems.

To recap, even with processed data from the time-frequency filtering procedure, the subspace time domain methods perform poorly with rapidly varying inputs. Including some frequency domain information in the subspace identification method will improve the estimates. Furthermore, enhancements are necessary in data processing for frequency domain data without assumptions of stationariness, time-invariance, periodicity, and white noise. Time-frequency filtering methods offer a solution. Other examples using a variety of estimation algorithms can be found in reference 22.

REFERENCES

1. Vernon, Lura, *In-flight Investigation of a Rotating Cylinder-Based Structural Excitation System for Flutter Testing*, NASA-TM-4512, June 1993.

2. Brenner, M., Rick Lind, and Dave Voracek, "Flight Flutter Testing Research at NASA Dryden," AIAA 97-0000, Apr. 1997.

3. Bowers, Albion H., Joseph W. Pahle, Joseph R. Wilson, Bradley C. Flick, and Richard L. Rood, *An Overview of the NASA F-18 High Alpha Research Vehicle,* NASA-TM-4772, Oct. 1996.

4. Brenner, Martin J., *Aeroservoelastic Modeling and Validation of a Thrust-Vectoring F/A-18 Aircraft*, NASA-TP-3647, Sept. 1996.

5. Schroeder, M. R., "Synthesis of Low Peak-Factor Signals and Binary Sequences with Low Auto-correlation," *IEEE Transactions on Information Theory*, vol. 16, pp. 85–89, Jan. 1970.

6. Van der Ouderaa, Edwin, Johan Schoukens, and Jean Renneboog, "Peak Factor Minimization of Input and Output Signals of Linear Systems," *IEEE Transactions on Instrumentation and Measurement*, vol. 37, no. 2, pp. 207–212, June 1988.

7. Strang, Gilbert and Truong Nguyen, *Wavelets and Filter Banks*, Wellesley-Cambridge Press, 1996.

8. Herley, Cormac, Jelena Kovacevic, Kannan Ramchandran, and Martin Vetterli, "Tilings of the Time-Frequency Plane: Construction of Arbitrary Orthogonal Bases and Fast Tiling Algorithms," *IEEE Transactions on Signal Processing*, vol. 41, no. 12, Dec. 1993.

9. Jones, Douglas L. and Richard G. Baraniuk, "An Adaptive Optimal-Kernel Time-Frequency Representation," *IEEE Transactions on Signal Processing*, vol. 43, no. 10, Oct. 1995.

10. Daubechies, Ingrid, *Ten Lectures on Wavelets*, Society for Industrial and Applied Mathematics, Philadelphia, PA, 1992.

11. Feron, Eric, and James D. Paduano, *Advanced Techniques for Flutter Clearance*, Annual report for NASA-MIT cooperative agreement no. DFRCU-95-025, Oct. 1996.

12. Lind, Rick and Marty Brenner, "Worst-Case Flutter Margins from F/A-18 Aircraft Aeroelastic Data," *38th AIAA Structures, Structural Dynamics and Materials Conference*, Apr. 1997.

13. Quatieri, Thomas F., Jr., "Short-Time Spectral Analysis with the Conventional and Sliding CZT," *IEEE Transactions on Acoustics, Speech, and Signal Processing*, vol. ASSP-26, no. 6, Dec. 1978.

14. Liu, Ketao, Robert N. Jacques, and David W. Miller, "Frequency Domain Structural System Identification by Observability Range Space Extraction," *Proceedings of the American Control Conference*, Baltimore, MD, vol. 1, pp. 107–111, 1994.

15. McKelvey, Tomas, Hüseyin Akçay, and Lennart Ljung, "Subspace-Based Multivariable System Identification from Frequency Response Data," *IEEE Transactions on Automatic Control*, vol. 41, no. 7, July 1996.

16. VanOverschee, Peter and Bart DeMoor, *Subspace Identification for Linear System Theory, Implementation, Applications*, Kluwer Academic Publishers, 1996.

17. Viberg, Mats, "Subspace-based Methods for the Identification of Linear Time-invariant Systems," *Automatica*, vol. 31, no. 12, Dec. 1995.

18. Misiti, Michel, Yves Misiti, Georges Oppenheim, and Jean-Michel Poggi, *Wavelet Toolbox User's Guide, For Use with MATLAB*, The Math Works, Inc., 1996.

19. Brenner, M., Rick Lind, and Dave Voracek, "Aeroservoelastic Model Identification with Multiple Inputs," AIAA 97-0000, Aug. 1997.

20. VanOverschee, Peter and Bart DeMoor, "Continuous-Time Frequency Domain Subspace System Identification," submitted for publication to *IEEE Transactions on Signal Processing*, 1995.

21. Duchesne, L., Eric Feron, James D. Paduano, and Marty Brenner, "Subspace Identification with Multiple Data Sets," *Proceedings of the 1996 AIAA Guidance, Navigation, and Control Conference*, San Diego, CA, May 1996.

22. Feron, E., L. Duchesne, A. Turevskiy, J. D. Paduano, and M. Brenner, "Time-Frequency Analysis for Transfer Function Estimation and Application to F18-SRA," submitted to the *Automatica*, Jan. 1997.

REPORT DOCUMENTATION PAGE

Form Approved
OMB No. 0704-0188

1. AGENCY USE ONLY (Leave blank)	2. REPORT DATE	3. REPORT TYPE AND DATES COVERED
	April 1997	Technical Memorandum

4. TITLE AND SUBTITLE

Wavelet Analyses of F/A-18 Aeroelastic and Aeroservoelastic Flight Test Data

5. FUNDING NUMBERS

522-32-34-00-RS-00-000

6. AUTHOR(S)

Martin J. Brenner

7. PERFORMING ORGANIZATION NAME(S) AND ADDRESS(ES)

NASA Dryden Flight Research Center
P.O. Box 273
Edwards, California 93523-0273

8. PERFORMING ORGANIZATION REPORT NUMBER

H-2164

9. SPONSORING/MONITORING AGENCY NAME(S) AND ADDRESS(ES)

National Aeronautics and Space Administration
Washington, DC 20546-0001

10. SPONSORING/MONITORING AGENCY REPORT NUMBER

NASA TM-4793

11. SUPPLEMENTARY NOTES

Presented at the 38th Structure, Structural Dynamics and Materials Conference Exhibit, AIAA, Kissimmee, Florida, April 7–10, 1997.

12a. DISTRIBUTION/AVAILABILITY STATEMENT

Unclassified—Unlimited
Subject Category 08

12b. DISTRIBUTION CODE

13. ABSTRACT (Maximum 200 words)

Time-frequency signal representations combined with subspace identification methods were used to analyze aeroelastic flight data from the F/A-18 Systems Research Aircraft (SRA) and aeroservoelastic data from the F/A-18 High Alpha Research Vehicle (HARV). The F/A-18 SRA data were produced from a wingtip excitation system that generated linear frequency chirps and logarithmic sweeps. HARV data were acquired from digital Schroeder-phased and sinc pulse excitation signals to actuator commands. Nondilated continuous Morlet wavelets implemented as a filter bank were chosen for the time-frequency analysis to eliminate phase distortion as it occurs with sliding window discrete Fourier transform techniques. Wavelet coefficients were filtered to reduce effects of noise and nonlinear distortions identically in all inputs and outputs. Cleaned reconstructed time domain signals were used to compute improved transfer functions. Time and frequency domain subspace identification methods were applied to enhanced reconstructed time domain data and improved transfer functions, respectively. Time domain subspace performed poorly, even with the enhanced data, compared with frequency domain techniques. A frequency domain subspace method is shown to produce better results with the data processed using the Morlet time-frequency technique.

14. SUBJECT TERMS

Aeroelasticity, Aeroservoelasticity, Aircraft vibration, Modal stability, Structural dynamics, System identification, Wavelet analysis

15. NUMBER OF PAGES

32

16. PRICE CODE

A03

17. SECURITY CLASSIFICATION OF REPORT	18. SECURITY CLASSIFICATION OF THIS PAGE	19. SECURITY CLASSIFICATION OF ABSTRACT	20. LIMITATION OF ABSTRACT
Unclassified	Unclassified	Unclassified	Unlimited